

Fig. 5.10 The critical nucleus size can be reduced even further by forming a low-energy coherent interface with one grain.

### Dislocations

The lattice distortion in the vicinity of a dislocation can assist nucleation in several ways. The main effect of dislocations is to reduce the  $\Delta G_s$ -contribution to  $\Delta G^*$  by reducing the total strain energy of the embryo. A coherent nucleus with a negative misfit, i.e. a smaller volume than the matrix, can reduce its  $\Delta G^*$  by forming in the region of compressive strain above an edge dislocation, whereas if the misfit is positive it is energetically favourable for it to form below the dislocation.

Nucleation on dislocations may also be assisted by solute segregation which can raise the composition of the matrix to nearer that of the precipitate. The dislocation can also assist in growth of an embryo beyond the critical size by providing a diffusion pipe with a lower  $\Delta G_m$ .

Dislocations are not very effective for reducing the interfacial energy contribution to  $\Delta G^*$ . This means that nucleation on dislocations usually requires rather good matching between precipitate and matrix on at least one plane, so that low-energy coherent or semicoherent interfaces can form. Ignoring strain energy effects, the minimum  $\Delta G^*$  is then achieved when the nucleus shape is the equilibrium shape given by the Wulff construction. When the precipitate and matrix have different crystal structures the critical nucleus should therefore be disc-like or needle-like as discussed in Section 3.4.2.

In fcc crystals the  $\frac{a}{2}\langle 110 \rangle$  unit dislocations can dissociate to produce a ribbon of stacking fault, e.g.

$$\frac{a}{2}[110] \rightarrow \frac{a}{6}[121] + \frac{a}{6}[21\bar{1}]$$

giving a stacking fault on  $(1\bar{1}1)$  separated by two Shockley partials. Since the stacking fault is in effect four close-packed layers of hcp crystal (Fig 3.59b) it can act as a very potent nucleation site for an hcp precipitate. This type of nucleation has been observed for the precipitation of the hexagonal transition phase  $\gamma'$  in Al–Ag alloys. Nucleation is achieved simply by the diffusion of silver atoms to the fault. Thus there will automatically be an orientation relationship between the  $\gamma'$  precipitate (fault) and the matrix of the type

$$\begin{aligned} (0001)_{\gamma'} // (1\bar{1}1)_{\alpha} \\ [11\bar{2}0]_{\gamma'} // [110]_{\alpha} \end{aligned}$$

which ensures good matching and low energy interfaces.

It should be noted that even in annealed specimens dislocation densities are often sufficiently high to account for any precipitate dispersion that is resolvable in the light microscope, i.e.  $\sim 1 \mu\text{m}^{-2}$ . Figure 5.11 shows an example of niobium carbonitride precipitates on dislocations in a ferritic iron matrix. This is a so-called dark-field electron microscope micrograph in which the precipitates are imaged bright and the matrix dark. The precipitates lie in rows along dislocations.

### Excess Vacancies

When an age-hardening alloy is quenched from a high temperature, excess vacancies are retained during the quench. These vacancies can assist nucleation by increasing diffusion rates, or by relieving misfit strain energies. They may influence nucleation either individually or collectively by grouping into small clusters.

Since  $\Delta G_d$  is relatively small for vacancies, nucleation will only take place when a reasonable combination of the following conditions is met: low interfacial energy (i.e. fully coherent nuclei), small volume strain energy, and

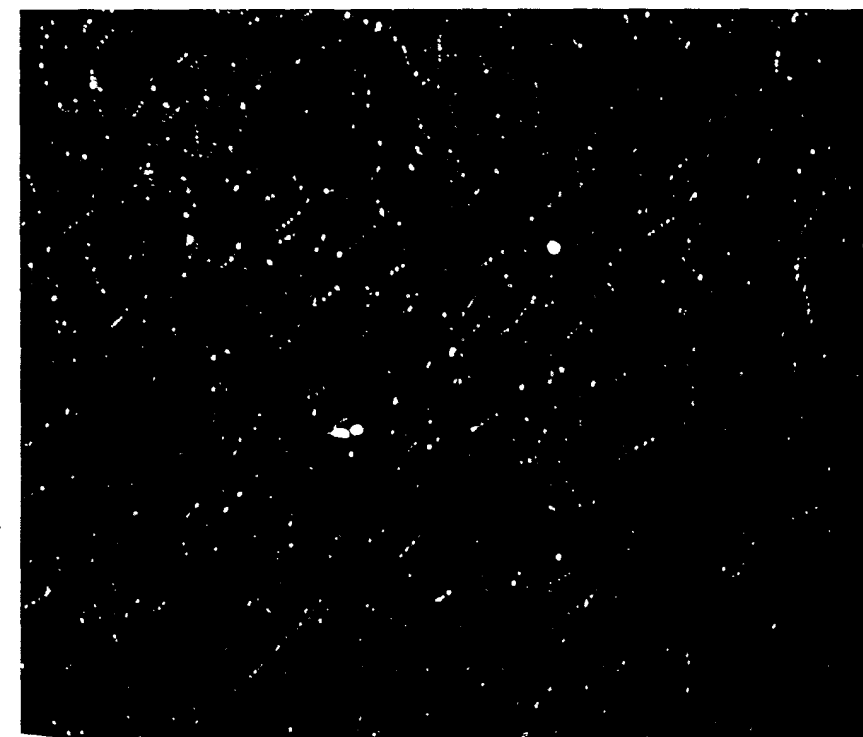


Fig. 5.11 Rows of niobium carbonitride precipitates on dislocations in ferrite ( $\times 108\,000$ ). (Dark-field electron micrograph in which the precipitates show up bright.)

high driving force. These are essentially the same conditions that must be fulfilled for homogeneous nucleation. Since individual vacancies or small clusters cannot be resolved with conventional transmission electron microscopy, evidence for the role of vacancies as heterogeneous nucleation sites is indirect (discussed later).

### 5.2.1 Rate of Heterogeneous Nucleation

If the various nucleation sites are arranged in order of increasing  $\Delta G_d$ , i.e. decreasing  $\Delta G^*$ , the sequence would be roughly

1. homogeneous sites
2. vacancies
3. dislocations
4. stacking faults
5. grain boundaries and interphase boundaries
6. free surfaces.

Nucleation should always occur most rapidly on sites near the bottom of the list. However the relative importance of these sites in determining the overall rate at which the alloy will transform also depends on the relative concentrations of the sites. For homogeneous nucleation every atom is a potential nucleation site, whereas only those atoms on grain boundaries, for example, can take part in boundary-assisted nucleation.

If the concentration of heterogeneous nucleation sites is  $C_1$  per unit volume, the heterogeneous nucleation rate will be given by an equation of the form

$$N_{\text{het}} = \omega C_1 \exp\left(-\frac{\Delta G_m}{kT}\right) \cdot \exp\left(-\frac{\Delta G^*}{kT}\right) \text{ nuclei m}^{-3}\text{s}^{-1} \quad (5.24)$$

This is plotted as a function of temperature in Fig. 5.12. Note that, as with heterogeneous nucleation in liquids, measurably high nucleation rates can be

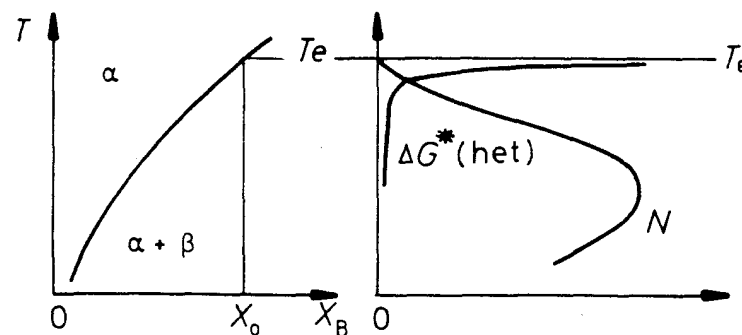


Fig. 5.12 The rate of heterogeneous nucleation during precipitation of  $\beta$  in alloy  $X_0$  as a function of undercooling.

obtained at very small driving forces. The relative magnitudes of the heterogeneous and homogeneous volume nucleation rates can be obtained by dividing Equation 5.11 by 5.24 giving

$$\frac{N_{\text{het}}}{N_{\text{hom}}} = \frac{C_1}{C_0} \exp\left(\frac{\Delta G_{\text{hom}}^* - \Delta G_{\text{het}}^*}{kT}\right) \quad (5.25)$$

(Differences in  $\omega$  and  $\Delta G_m$  are not so important and have been ignored.) Since  $\Delta G^*$  is always smallest for heterogeneous nucleation the exponential factor in the above equation is always a large quantity which favours a high heterogeneous nucleation rate. However, the factor  $(C_1/C_0)$  must also be taken into account, i.e. the number of atoms on heterogeneous sites relative to the number within the matrix. For grain boundary nucleation

$$\frac{C_1}{C_0} = \frac{\delta}{D} \quad (5.26)$$

where  $\delta$  is the boundary thickness and  $D$  is the grain size. For nucleation on grain edges and corners  $(C_1/C_0)$  becomes reduced even further to  $(\delta/D)^2$  and  $(\delta/D)^3$ . Therefore for a  $50 \mu\text{m}$  grain size taking  $\delta$  as  $0.5 \text{ nm}$  gives  $\delta/D \approx 10^{-5}$ . Consequently grain boundary nucleation will dominate over homogeneous nucleation if the boundary is sufficiently potent to make the exponential term in Equation 5.23 greater than  $10^5$ . Values for  $C_1/C_0$  for other sites are listed in Table 5.1.

In general the type of site which gives the highest volume nucleation rate will depend on the driving force ( $\Delta G_v$ ). At very small driving forces, when activation energy barriers for nucleation are high, the highest nucleation rates will be produced by grain-corner nucleation. As the driving force increases, however, grain edges and then boundaries will dominate the transformation. At very high driving forces it may be possible for the  $(C_1/C_0)$  term to dominate and then homogeneous nucleation provides the highest nucleation rates. Similar considerations will apply to the relative importance of other heterogeneous nucleation sites.

The above comments concerned nucleation during isothermal transformations when the specimen is held at a constant temperature. If nucleation occurs during continuous cooling the driving force for nucleation will increase with time. Under these conditions the initial stages of the transformation will be dominated by those nucleation sites which can first produce a measurable volume nucleation rate. Considering only grain boundaries again, if  $\gamma_{\alpha\alpha}/\gamma_{\alpha\beta}$  is high, noticeable transformation will begin first at the grain corners, whereas if the grain boundary is less potent ( $\gamma_{\alpha\alpha}/\gamma_{\alpha\beta}$  smaller) nucleation may not be possible until such high driving forces are reached that less favourable heterogeneous or even homogeneous nucleation sites dominate. This will not of course exclude precipitation on potent heterogeneous sites, but they will make only a very small contribution to the total nucleation rate.

Table 5.1  $C_1/C_0$  for Various Heterogeneous Nucleation Sites

Grain boundary	Grain edge	Grain corner	Dislocations	Excess vacancies
$D = 50 \mu\text{m}$	$D = 50 \mu\text{m}$	$D = 50 \mu\text{m}$	$10^5 \text{ mm}^{-2}$	$X_v = 10^{-6}$
$10^{-5}$	$10^{-10}$	$10^{-15}$	$10^{-8}$	$10^{-6}$

### 5.3 Precipitate Growth

As explained above, the successful critical nuclei are those with the smallest nucleation barrier, i.e. the smallest critical volume. In the absence of strain-energy effects the precipitate shape satisfying this criterion is that which minimizes the total interfacial free energy. Thus nuclei will usually be bounded by a combination of coherent or semicoherent facets and smoothly curved incoherent interfaces. For the precipitate to grow these interfaces must migrate and the shape that develops during growth will be determined by the relative migration rates. As explained in Section 3.5.1, when the two phases have different crystal structures semicoherent interfaces have very low mobility and are forced to migrate by a ledge mechanism. Incoherent interfaces on the other hand are highly mobile. If there are problems in maintaining a constant supply of ledges the incoherent interfaces will be able to advance faster than the semicoherent interface and a nucleus with one plane of good matching should grow into a thin disc or plate as shown in Fig. 5.13. This is the origin of the so-called Widmanstätten morphology<sup>12</sup>.

The next few sections will be concerned with developing an approximate quantitative treatment for the ledge mechanism and for the rate of migration of curved incoherent interfaces, but before treating these two cases it is useful to begin with the simpler case of a planar incoherent interface.

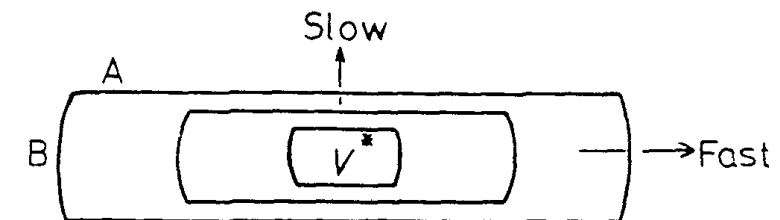


Fig. 5.13 The effect of interface type on the morphology of a growing precipitate. (A) Low-mobility semicoherent interfaces. (B) High-mobility incoherent interfaces.

#### 5.3.1 Growth behind Planar Incoherent Interfaces

It will be apparent from the above discussion that planar interfaces in crystalline solids will usually not be incoherent. However, one situation where approximately planar incoherent interfaces may be found is after grain-boundary nucleation. If many incoherent nuclei form on a grain boundary they might subsequently grow together to form a slab of  $\beta$  precipitate as shown in Fig. 5.14.

Imagine that such a slab of solute-rich precipitate has grown from zero thickness and that the instantaneous growth rate is  $v$ . Since the concentration of solute in the precipitate ( $C_\beta$ ) is higher than in the bulk ( $C_0$ ) the matrix adjacent to the precipitate will be depleted of solute as shown. Also since the interface is incoherent diffusion-controlled growth and local equilibrium at

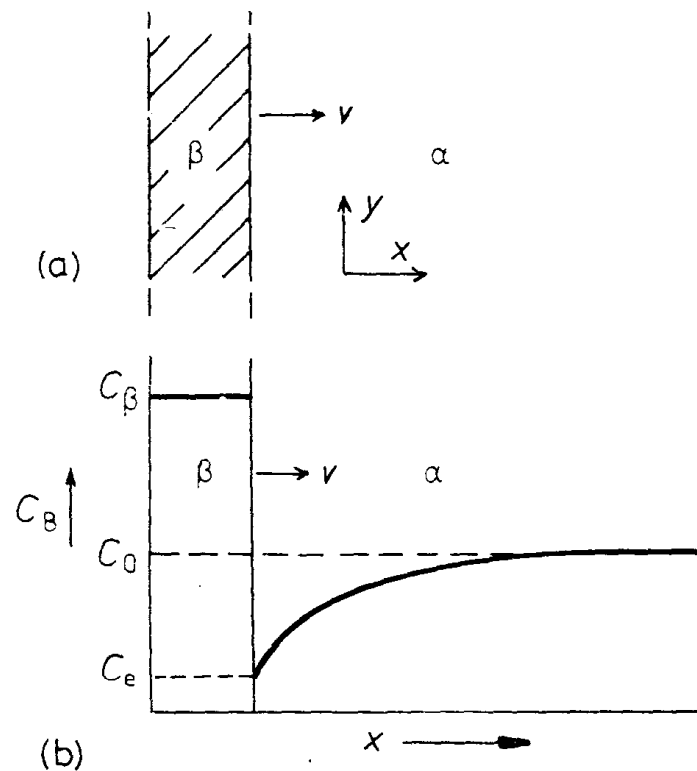


Fig. 5.14 Diffusion-controlled thickening of a precipitate plate.

the interface can be assumed, i.e. the solute concentration in the matrix adjacent to the  $\beta$  will be the equilibrium value  $C_e$ . The growth rate ( $v$ ) will depend on the concentration gradient at the interface  $dC/dx$ .

For unit area of interface to advance a distance  $dx$  a volume of material  $1 \cdot dx$  must be converted from  $\alpha$  containing  $C_e$  to  $\beta$  containing  $C_\beta$  moles of B per unit volume, i.e.  $(C_\beta - C_e)dx$  moles of B must be supplied by diffusion through the  $\alpha$ . The flux of B through unit area in time  $dt$  is given by  $D(dC/dx)dt$ , where  $D$  is the *interdiffusion* coefficient (or *interstitial diffusion* coefficient). Equating these two quantities gives

$$v = \frac{dx}{dt} = \frac{D}{C_\beta - C_e} \cdot \frac{dC}{dx} \quad (5.27)$$

As the precipitate grows solute must be depleted from an ever-increasing volume of matrix so that  $dC/dx$  in the above equation decreases with time. To make this quantitative, consider a simplified approach originally due to Zener<sup>2</sup>. If the concentration profile is simplified to that shown in Fig. 5.15  $dC/dx$  is given by  $\Delta C_0/L$  where  $\Delta C_0 = C_0 - C_e$ . The width of the diffusion zone  $L$  can be obtained by noting that the conservation of solute requires the two shaded areas in Fig. 5.15 to be equal, i.e.

$$(C_\beta - C_0)x = L\Delta C_0/2$$

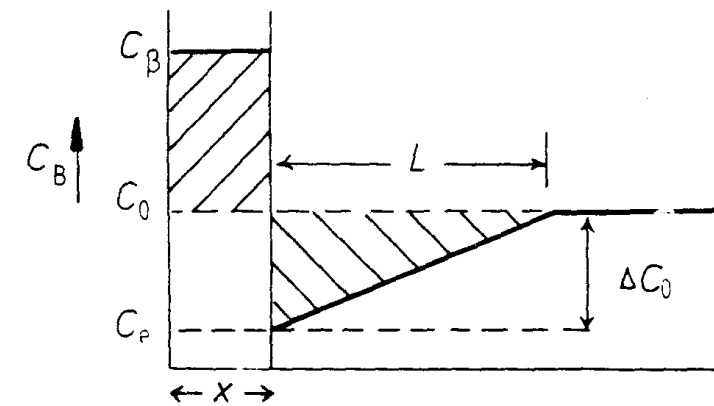


Fig. 5.15 A simplification of the concentration profile.

where  $x$  is the thickness of the slab. The growth rate therefore becomes

$$v = \frac{D(\Delta C_0)^2}{2(C_\beta - C_e)(C_\beta - C_0)x} \quad (5.28)$$

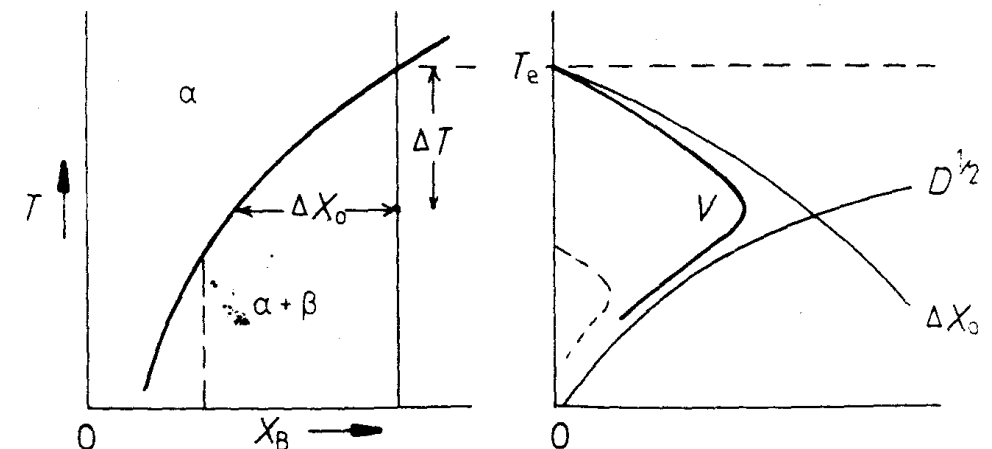
If it is assumed that the molar volume ( $V_m$ ) is a constant, the concentrations in the above equation can be replaced by mole fractions ( $X = CV_m$ ). Furthermore, for the sake of simplicity it can often be assumed that  $C_\beta - C_0 \approx C_\beta - C_e$ . Integration of Equation 5.28 then gives

$$x = \frac{\Delta X_0}{(X_\beta - X_e)} \sqrt{Dt} \quad (5.29)$$

and

$$v = \frac{\Delta X_0}{2(X_\beta - X_e)} \sqrt{\frac{D}{t}} \quad (5.30)$$

where  $\Delta X_0 = X_0 - X_e$  (Fig. 5.16) is the supersaturation prior to precipitation.

Fig. 5.16 The effect of temperature and position on growth rate,  $v$ .

The following points are important to note regarding these equations.

1.  $x \propto \sqrt{(Dt)}$ , i.e. precipitate thickening obeys a parabolic growth law.
2.  $v \propto \Delta X_0$ , i.e. for a given time the growth rate is proportional to the supersaturation.
3.  $v \propto \sqrt{(D/t)}$ .

The effect of alloy composition and temperature on growth rate is illustrated in Fig. 5.16. Growth rates are low at small undercoolings due to small supersaturation  $\Delta X_0$  but are also low at large undercoolings due to slow diffusion. A maximum growth rate will occur at some intermediate undercooling.

When the diffusion fields of separate precipitates begin to overlap Equation 5.30 will no longer apply, but growth will decelerate more rapidly and finally cease when the matrix concentration is  $X_e$  everywhere, Fig. 5.17.

Although these equations are only approximate and were derived for a planar interface, the conclusions are not significantly altered by more thorough treatments or by allowing curved interfaces. Thus it can be shown that

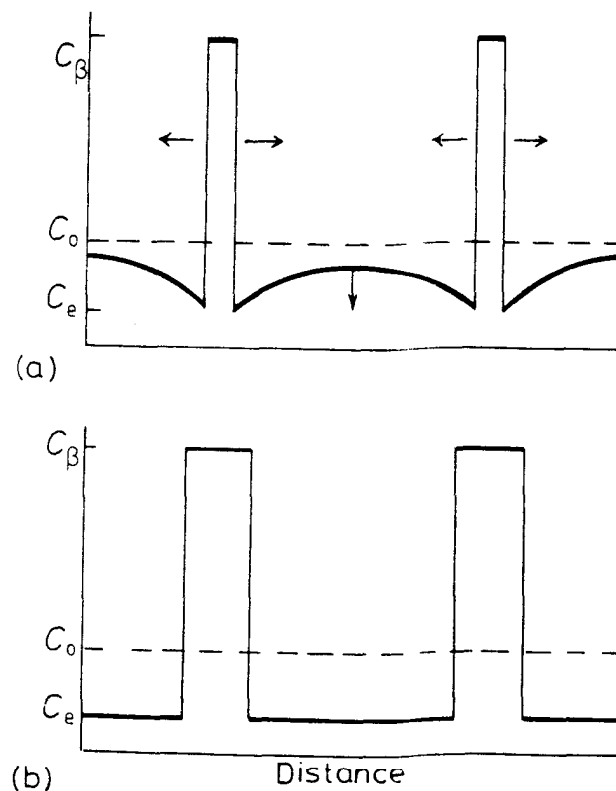


Fig. 5.17 (a) Interference of growing precipitates due to overlapping diffusion fields at later stage of growth. (b) Precipitate has stopped growing.

any linear dimension of a spheroidal precipitate increases as  $\sqrt{(Dt)}$  provided all interfaces migrate under volume diffusion control.

Usually grain boundary precipitates do not form a continuous layer along the boundary but remain as isolated particles. The growth of such precipitates can occur at rates far greater than allowed by volume diffusion. The reason for this is that the grain boundary can act as a collector plate for solute as shown in Fig. 5.18.<sup>22</sup> Growth of such a so-called grain-boundary allotriomorph involves three steps: (1) volume diffusion of solute to the grain boundary; (2) diffusion of solute along the grain boundary with some attachment at the precipitate rim; and (3) diffusion along the  $\alpha/\beta$  interfaces allowing accelerated thickening. This mechanism is of greatest significance when substitutional diffusion is involved. In the case of interstitial solutions diffusion short circuits are comparatively unimportant due to the high volume diffusion rates.

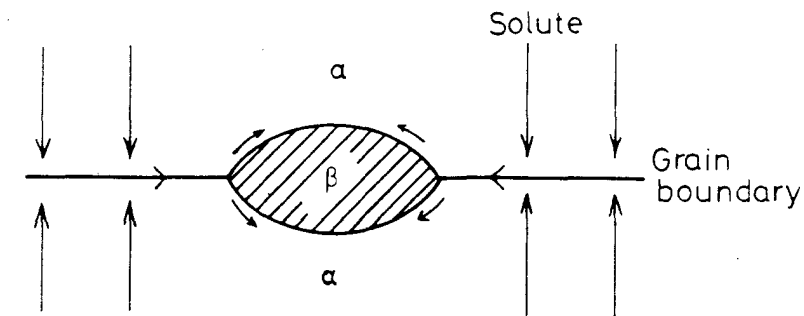


Fig. 5.18 Grain-boundary diffusion can lead to rapid lengthening and thickening of grain boundary precipitates.

### 5.3.2 Diffusion-Controlled Lengthening of Plates or Needles

Imagine now that the  $\beta$  precipitate is a plate of constant thickness having a cylindrically curved *incoherent* edge of radius  $r$  as shown in Fig. 5.19a. Again the concentration profile across the curved interface will appear as shown in Fig. 5.19b, but now, due to the Gibbs-Thomson effect, the equilibrium concentration in the matrix adjacent to the edge will be increased to  $C_r$ . The concentration gradient available to drive diffusion to the advancing edge is therefore reduced to  $\Delta C/L$  where  $\Delta C = C_0 - C_r$  and  $L$  is a characteristic diffusion distance. The diffusion problem in this case is more complex as diffusion occurs radially. However, solution of the relevant equations shows that  $L$  is given by  $kr$  where  $k$  is a numerical constant ( $\sim 1$ ). By analogy with Equation 5.27, therefore, the lengthening rate will be given by

$$v = \frac{D}{C_\beta - C_r} \cdot \frac{\Delta C}{kr} \quad (5.31)$$

The composition difference available to drive diffusion will depend on the tip radius as shown in Fig. 5.20. With certain simplifying assumptions it can

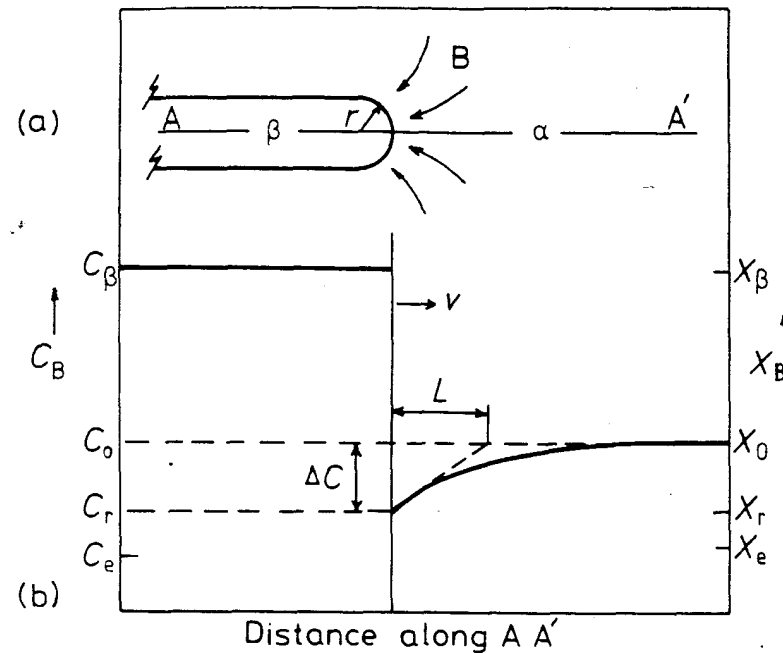


Fig. 5.19 (a) The edge of a plate-like precipitate. (b) A concentration profile along AA' in (a).

be shown that

$$\Delta X = \Delta X_0 \left( 1 - \frac{r^*}{r} \right) \quad (5.32)$$

where  $\Delta X = X_0 - X_r$ ,  $\Delta X_0 = X_0 - X_e$  and  $r^*$  is the critical nucleus radius, i.e. the value of  $r$  required to reduce  $\Delta X$  to zero. Again, assuming constant molar volume, the above equations can be combined to give

$$v = \frac{D \Delta X_0}{k(X_\beta - X_r)} \cdot \frac{1}{r} \left( 1 - \frac{r^*}{r} \right) \quad (5.33)$$

This equation will apply as long as there is no decrease in supersaturation far from the interface due to other precipitates. The difference between this equation and Equation 5.30 is that for a given plate thickness the lengthening rate should be constant, i.e.  $x \propto t$  (linear growth).

Although the above equations were developed for the lengthening of a plate, the same equations can be derived for the lengthening of a needle under diffusion-controlled growth. The only difference is that the edge of a needle has a spherical tip so that the Gibbs-Thomson increase in free energy is  $2\gamma V_m/r$  instead of  $\gamma V_m/r$ . The value of  $r^*$  in Equation 5.33 will, therefore, be different for a plate and a needle.

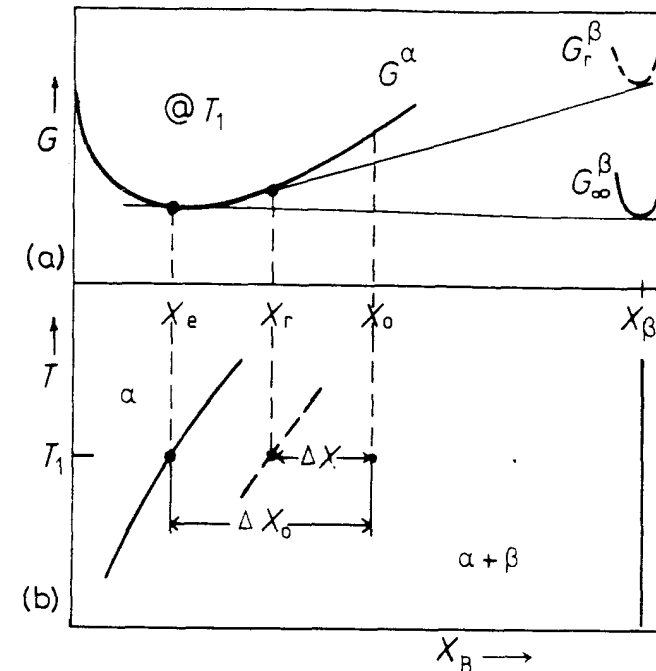


Fig. 5.20 The Gibbs-Thomson effect. (a) Free energy curves at  $T_1$ . (b) Corresponding phase diagram.

The above treatment only applies to plates or needles that lengthen by a volume diffusion-controlled continuous growth process. This is a reasonable assumption for the curved ends of needles, but in the case of plate-like precipitates the edges are often faceted and are observed to migrate by a ledge mechanism. Atoms can then only attach at the ledges and new equations must be derived as discussed below.

Another source of deviation between theory and practice is if solute can be transported to the advancing precipitate edges by short-circuit diffusion in the broad faces of the precipitate plate.

### 5.3.3 Thickening of Plate-like Precipitates

The treatment given in Section 5.3.1 for a planar incoherent interface is only valid for interfaces with high accommodation factors. In general this will not be the case for the broad faces of plate-like precipitates which are semicoherent and are restricted to migrate by the lateral movement of ledges.

For simplicity, imagine a plate-like precipitate that is thickening by the lateral movement of linear ledges of constant spacing  $\lambda$  and height  $h$ , Fig. 5.21. It can readily be seen that the half-thickness of the plate should

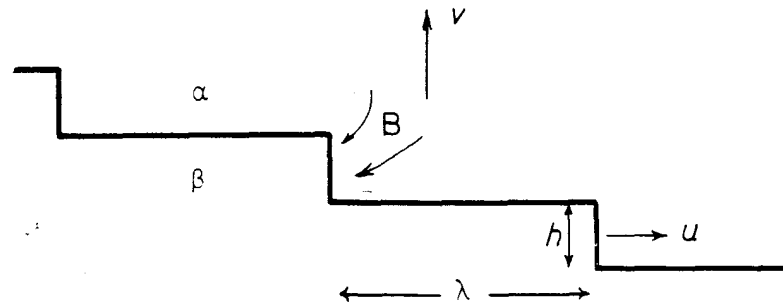


Fig. 5.21 Thickening of plate-like precipitates by ledge mechanism.

increase at a rate  $v$  given by

$$v = \frac{uh}{\lambda} \quad (5.34)$$

where  $u$  is the rate of lateral migration.

The problem of ledge migration is very similar to that of plate lengthening. The necessary composition changes required for precipitate growth must be achieved by long-range diffusion to and from the ledges as shown in Fig. 5.21. If the edges of the ledges are incoherent the matrix composition in contact with the ledges will be  $X_e$  and growth will be diffusion controlled. A similar treatment to that given in Section 5.3.2 then gives the rate of lateral migration as<sup>3</sup>

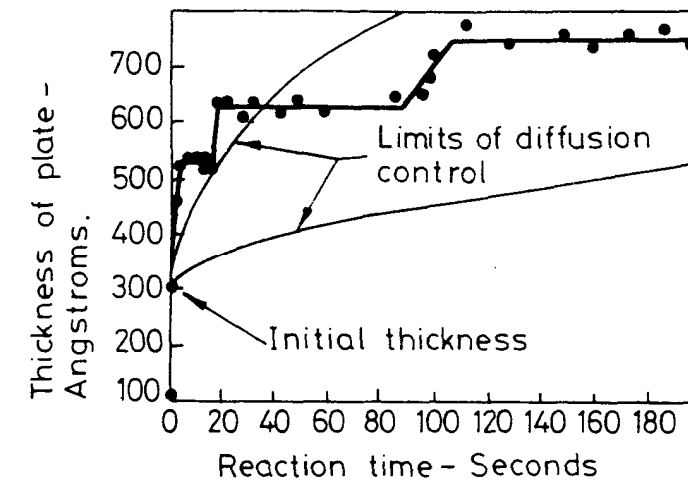
$$u = \frac{D\Delta X_0}{k(X_\beta - X_e)h} \quad (5.35)$$

This is essentially the same as Equation 5.33 for the lengthening of a plate with  $h \approx r$  and  $X_r = X_e$ , i.e. no Gibbs-Thomson effect. Combining the above equations shows that the thickening rate is independent of  $h$  and given by

$$v = \frac{D\Delta X_0}{k(X_\beta - X_e)\lambda} \quad (5.36)$$

Thus, provided the diffusion fields of different precipitates do not overlap, the rate at which plates thicken will be inversely proportional to the interledge spacing  $\lambda$ . The validity of Equation 5.36 is dependent on there being a constant supply of ledges. As with faceted solid/liquid interfaces, new ledges can be generated by various mechanisms such as repeated surface nucleation, spiral growth, nucleation at the precipitate edges, or from intersections with other precipitates. With the exception of spiral growth, however, none of these mechanisms can maintain a supply of ledges with constant  $\lambda$ .

By using hot-stage transmission electron microscopy it is possible to measure the thickening rates of individual precipitate plates. Figure 5.22 shows results obtained from a  $\gamma$  plate in the Al-Ag system<sup>4</sup>. It can be seen that there

Fig. 5.22 The thickening of a  $\gamma$  plate in an Al-15 wt% Ag alloy at 400 °C. (From C. Laird and H.I. Aaronson, *Acta Metallurgica* 17 (1969) 505.)

are appreciable intervals of time when there is no perceptible increase in plate thickness followed by periods when the thickness increases rapidly as an interfacial ledge passes. The two smooth lines in the figure are upper and lower limits for the rate of thickening for a planar incoherent interface in the same system, assuming diffusion control. The ledge mechanism is clearly a very different process. The fact that there is no perceptible increase in thickness except when ledges pass is strong evidence in favour of the immobility of semicoherent interfaces. It can also be seen that the thickening rate is not constant implying that ledge nucleation is rate controlling.

Measurements on precipitates in other systems indicate that even within the same system the thickness/time relationship can vary greatly from plate to plate, presumably depending on differences in the ease of nucleation of new ledges.

#### 5.4 Overall Transformation Kinetics—TTT Diagrams

The progress of an isothermal phase transformation can be conveniently represented by plotting the fraction transformation ( $f$ ) as a function of time and temperature, i.e. a TTT diagram as shown in Fig. 5.23a for example. For transformations of the type  $\alpha \rightarrow \beta$ ,  $f$  is just the volume fraction of  $\beta$  at any time. For precipitation reactions  $\alpha' \rightarrow \alpha + \beta$ ,  $f$  can be defined as the volume of  $\beta$  at time  $t$  divided by the final volume of  $\beta$ . In both cases  $f$  varies from 0 to 1 from the beginning to the end of the transformation, Fig. 5.23b.

Among the factors that determine  $f(t, T)$  are the nucleation rate, the growth rate, the density and distribution of nucleation sites, the overlap of diffusion fields from adjacent transformed volumes, and the impingement of